# Heavy versus Light Lanthanide Selectivity for Graphene Oxide Films is Concentration Dependent

*Amanda J. Carr, Seung Eun Lee, Ahmet Uysal\**

Chemical Sciences and Engineering Division, Argonne National Laboratory, Lemont, IL 60439

ABSTRACT

Rare earths are important materials in various technologies such as catalysis and optoelectronics. Graphene oxide (GO) is a promising material for separation applications, including the isolation of lanthanides from complex mixtures. Previous works using fatty acid monolayers have demonstrated preferential heavy versus light lanthanide adsorption, which has been attributed to differences in lanthanide ion size. In this work, we used interfacial X-ray fluorescence measurements to reveal that GO thin films at the air/water interface have no lanthanide selectivity for dilute subphases. However, at high subphase concentrations ~8x more $Lu^{3+}$ adsorb than $La^{3+}$. By comparing GO results with an ideal monolayer with a carboxylic acid headgroup, arachidic acid (AA), we demonstrate that the number of $Lu^{3+}$ adsorbed at GO is significantly higher than the number needed to compensate the surface charge. Vibrational sum frequency generation (SFG) spectroscopy results on both GO thin films and AA monolayers reveal a red-shifted SFG signal in the OH region, which we attribute to partial dehydration of the adsorbed ions. Liquid surface X-ray reflectivity data show that the GO thin film structure does not significantly change between the very dilute and concentrated subphases. We speculate that the functional groups of both GO and AA facilitate cation dehydration, which is essential for ion adsorption. Heavy lanthanide $Lu^{3+}$ has stronger ion-ion correlations that can overcome electrostatic repulsion between cations at higher concentrations compared to light lanthanide $La^{3+}$, meaning GO and AA can overcharge with $Lu^{3+}$. Lastly, the layered structure of the GO films and reactive chemical nature of GO itself can accommodate ion adsorption.

Isolating rare earths from complex mixtures is critical for a range of applications including catalysis and petroleum refining, medical imaging, permanent magnet fabrication, optoelectronics, and green technology development among others.[1-4] Graphene oxide (GO) is a promising[5] two-dimensional amphiphile due to its $sp^2$ hybridized carbon backbone decorated with oxygen functional groups including carboxylic acid, epoxy, and hydroxyl groups.[6] The exact chemical and physical structures vary depending on the synthesis[7] but GO usually exists as flakes with hydrophobic basal planes and hydrophilic edges.[8, 9] Experimental and computational works have investigated rare earth,[10-13] actinide,[11, 14-18] and other metal separations[19-22] using GO, typically through bulk adsorption of the metal ions onto the GO flakes or filtration via GO membranes consisting of stacked GO flakes. Arguably, the nanoscale interactions governing the success of these separations occurs in the small, interfacial region formed between the GO flakes and liquid. Recent works have probed this interface by creating GO thin films directly on aqueous subphases[23-28] and a recent work by our group connected interfacial interactions with GO to rare earth metal separation performance using GO membranes.[29]

Interestingly, the extraction efficiency of metals across the lanthanide series varies even though nearly all ions are trivalent in typical aqueous conditions.[1, 2, 30-32] These differences have been attributed to lanthanide contraction,[33, 34] where the atomic radius of the metal decreases as the atomic number increases. This small but important variation in the ion size strongly affects hydration structures,[35] coordination chemistry,[36] and solvation enthalpies.[37] Indeed, studies have probed changes in the hydration structure of the lanthanides across the series.[38] X-ray scattering and molecular dynamics simulations[35] have shown a gradual transition from ~9 to ~8 waters in the first coordination shell from $La^{3+}$ to $Lu^{3+}$. The hydration structure of ions at the air/water interface is directly relevant to separation efforts, as ions may undergo partial or total dehydration during

adsorption[32, 39-41]. Recently, our group studied $Nd^{3+}$ adsorption to arachidic acid (AA) films using vibrational sum frequency generation spectroscopy (SFG) and observed a red-shifted signal within the water region, which was attributed to the partial dehydration of adsorbed $Nd^{3+}$ ions.[39] SFG is an inherently surface-specific technique that is well-suited to understand local water structures near the air/water interface, as signal is only generated when centrosymmetry is broken (Figure 1).[40-44]

In this work, we consider both light lanthanide $La^{3+}$ and heavy lanthanide $Lu^{3+}$ adsorption to a GO thin film and an ideal AA monolayer at the air/water interface to understand the effects of ion size on adsorption and local water structure. AA serves as a model monolayer composed of well-organized carboxylic acid headgroups each with a hydrocarbon tail. This comparison allows quantifying the density of carboxylic acid groups on GO and resolves the ambiguities due to the interference effects in the SFG signal.[26] Surface X-ray fluorescence near total reflection (XFNTR) measurements on GO and AA monolayers (Figure 1) allow quantitative determination of adsorbed $La^{3+}$ and $Lu^{3+}$ ions[45] and reveal that GO thin films adsorb 8.3x more $Lu^{3+}$ versus $La^{3+}$ when placed on a high concentration subphase. By comparing this adsorbed ion density to that of AA and examining the thin film structure with liquid surface X-ray reflectivity (XR) (Figure 1), we show that the GO films are overcharging for $Lu^{3+}$, i.e. significantly more $Lu^{3+}$ ions adsorb than the amount needed to compensate the surface charge of GO. However, $La^{3+}$ ions do not show overcharging. Strikingly, for dilute subphases, $La^{3+}$ and $Lu^{3+}$ adsorption to GO thin films is nearly identical with no noticeable selectivity. Additionally, the XFNTR measurements explicitly show AA monolayer overcharging when $Lu^{3+}$ is present while $La^{3+}$ adsorption follows the expected charge compensation. This is the first time, to the best of our knowledge, that overcharging on AA with only a heavy lanthanide has been demonstrated. These results are coupled with SFG

4

measurements that show the emergence of a signal attributed to partially dehydrated adsorbed ions that is present for both GO thin films and AA monolayers. We posit the functional groups of GO and AA facilitate partial ion dehydration and allow adsorption, as evidenced by our SFG results. Lastly, we speculate GO thin films can accommodate more adsorbed ions because of their complex layered structure and the reactive chemistry of GO.
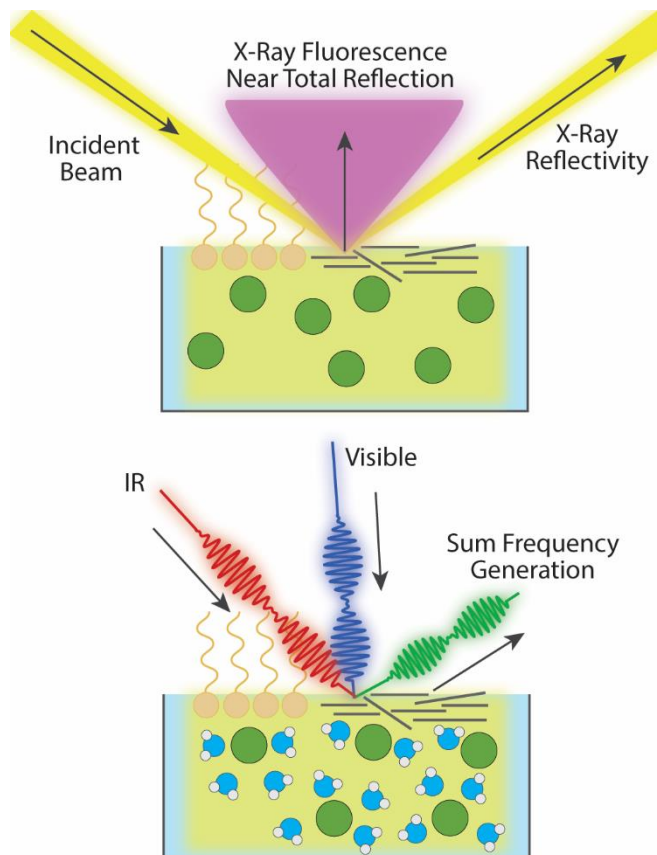


**Figure 1**. Experimental cartoon showing arachidic acid (AA, tan) monolayers and graphene oxide (GO, gray) thin films at the air/water interface. X-ray fluorescence (top), X-ray reflectivity (top), and sum frequency generation spectroscopy (bottom) are interface–specific techniques that detail the adsorbed ion density, monolayer or film structure, and water organization, respectively.

**Experimental Section**

*Materials and sample preparation*

All samples were prepared using ultrapure water (resistivity = 18.2 MΩ, Millipore, Synergy Water Purification system). We considered two surfactants: arachidic acid (AA) and graphene oxide (GO). 1 mM AA samples (Sigma Aldrich) were prepared using 3:1 chloroform:methanol (v:v, Sigma Aldrich) and were stored at 0°C. GO samples were made by sonicating a stock solution of 10 mg/mL GO (Standard Graphene) for 5 minutes and then diluting to 1 mg/mL with water. Samples were diluted again 1:5 with anhydrous methanol (Sigma Aldrich), sonicated for 1 hour, and lastly filtered through a 1.2 µm syringe filter. Metal solution samples were prepared using $LaCl_3 \cdot 7H_2O$ (99.999% trace metals basis) and $LuCl_3 \cdot 6H_2O$ ($\geq$ 99.99% trace metals basis) (Sigma Aldrich).

*Synchrotron x-ray measurements*

Liquid surface X-ray reflectivity (XR) and X-ray fluorescence near total reflection (XFNTR) measurements were completed at Sector 15ID-C, ChemMatCARS, at the Advanced Photon Source at Argonne National Laboratory. The incident X-ray beam at 10 keV is focused using various optics and the final size is 2 mm horizontal by 40 µm vertical set using slits.

Samples are prepared in a Teflon-coated Langmuir trough, with a single barrier and a pressure sensor (Nima) equipped with a clean Wilhelmy plate made of chromatography paper, placed inside a containment box. A custom glass slab cleaned using Nochromix is placed in the trough to reduce the trough volume to 200 mL. The trough is thoroughly cleaned before each sample by wiping with chloroform and alcohol and then rinsing 2-3 times with clean water. 200 mL of the liquid subphase is placed in the trough and the surface is cleaned to eliminate contamination. After cleaning, the surfactant, either AA or GO, is slowly spread on top of the subphase using an

appropriately sized glass syringe (Hamilton). For these measurements, we spread 150 μL of AA

and 200 μL of GO. The barrier is slowly closed until the target surface pressure is obtained, 10

mN/m for AA and 20 mN/m for GO. The final area depends on the surfactant. The containment

chamber is purged with He gas, which reduces X-ray damage to the sample during the

measurement and minimized unwanted background scattering in air. The He is bubbled through

water prior to purging to keep the humidity consistent.

*Liquid surface x-ray reflectivity measurements and fitting*

After aligning the liquid sample height, reflectivity data is collected by measuring the specular

reflection of the incident X-ray beam off the liquid surface as a function of the momentum transfer

$Q_z = (4\pi/\lambda) \sin(2\alpha/2)$ where $\lambda$ is the wavelength of the incident beam, 1.24 Å, and $\alpha$ is the

angle between the incident beam and sample surface. The reflections are measured on a Pilatus

200K detector. The sample is horizontally shifted at different points during the scan to reduce

beam damage effects and a few data points are re-collected to check reproducibility.

Obtained XR data for GO are modelled using 3 slabs each with its own thickness and electron

density, and a global roughness parameter. The roughness of these non-sharp, layered interfaces is

dominated by surface capillary waves hence the roughness of each slab was set to be equal through

the global roughness parameter. The slab parameters were determined using the recursive Parratt

formulism via least-squares fitting to the following merit function (Equation 1):

$$\chi^2 = \sum_{i=1}^{N} \frac{\left(R_{calc_i} - R_{exp_i}\right)^2}{\gamma_i^2} \tag{1}$$

where $R_{calc}$ is the calculated reflectivity, $R_{exp}$ is the experimentally measured reflectivity, and $\gamma$

is the uncertainty for each slab $i$. Reflectivity data were fit using StochFit.[46]

*X-ray fluorescence near total reflection measurements and fitting*

Fluorescence intensities were collected on a Vortex-60EX multi-cathode energy dispersive detector positioned 10.4 mm perpendicular to the liquid surface sample. Detector calibration data were collected by measuring a 20 mM metal subphase sample without a surfactant. Measured fluorescence data were collected on prepared samples with a surfactant, either AA or GO. All fluorescence energies are recorded simultaneously over $Q_Z$ and the target subphase ion emission energy is extracted after the measurement by fitting the emission energy to a Gaussian peak with a polynomial background. Consequently, we can assess subphase metal ion contamination, which was insignificant in our measurements. This process is repeated for each measured value of $Q_Z$.

XFNTR data are fit by calculating the penetration depth and area of the incident X-ray based on the beam parameters and fitting the surface density of fluorescent ions necessary to generate signal from that calculated area. Because the beam footprint on the liquid sample is always larger than the area of the detector, only the penetration depth changes as $Q_z$ varies. We measure $Q_z$ around the critical angle $Q_C = 4\sqrt{\pi r_{e-}\Delta\rho}$ where $r_{e-}$ is the classical radius of an electron and $\Delta\rho$ is the electron density contrast between the liquid subphase and air. For these samples, $Q_C \sim 0.022$ Å$^{-1}$. At $Q_Z < Q_C$, the signal undergoes total external reflection and fluorescence signal from ions at the interface is enhanced. At $Q_Z > Q_C$, fluorescence signal is generated from the bulk and interface.[45] Data were fitted using liquid surface software freely available from ChemMatCARS.

After fitting the XFNTR data to determine the surface density of adsorbed ions, data were plotted over concentration for LaCl$_3$ and LuCl$_3$ for both AA and GO. These concentration isotherms were fitted to a modified Langmuir adsorption model (Equation 2):

$$\theta = A + \theta_{Max}\left(\frac{K_B C}{1 + K_B C}\right) \tag{2}$$

where $\theta$ is the absorbed ion coverage, $\theta_{Max}$ is the maximum adsorbed ion coverage, $K_B$ is the adsorbed ion binding affinity, $C$ is the subphase concentration, and $A$ is a vertical offset.[47]

*Sum frequency generation spectroscopy measurements*

SFG samples were prepared by slowly spreading a small amount of either AA or GO dropwise on an approximately 22 mL subphase in a polytetrafluoroethylene dish (inner diameter of 60 mm and a height of 20 mm) while monitoring the surface pressure with a sensor (Nima) equipped with clean chromatography paper. AA was added until the surface pressure reached 10 mN/m and GO was added until the surface pressure reached 20 mN/m. All data were collected at room temperature under regular air.

SFG measurements were completed using an EKSPLA system, which has been described in detail elsewhere.[40, 43, 48] Briefly, an amplified Nd:YAG laser produces 20 ps pulses with 28 mJ power centered at 1064 nm at a rate of 50 Hz. This 1063 nm beam is split into two 532 nm beams. One is used as the visible light source to measure the sample, and the other is used to generate a tunable IR signal using the original 1064 nm beam. These two signals are overlapped spatially and temporarily at the liquid surface to generate the SFG signal. The 532 nm beam was attenuated to 200 μJ and the IR beam was attenuated to 100 μJ power during the measurements. The angles of incidence for the 532 nm and IR beams are 60° and 55° normal to the surface, respectively. The generated SFG signal is detected by a photomultiplier tube connected to a monochromator. Each spectrum is measured over the vibrational water range from 2800-3200 cm$^{-1}$ using 4 cm$^{-1}$ steps. Each datum point is the average of 300 laser shots. To avoid sample damage, the sample is rotated after every three frequency steps. All presented SFG data are normalized to a reference z-cut quartz (MTI Corporation). Data are collected with a SSP polarization.

**Results and Discussion**

*La^{3+} and Lu[3+] ion adsorption to graphene oxide and arachidic acid*

To understand the impacts of ion size on adsorption, we determined the adsorbed La^{3+} and Lu[3+] ion surface density for GO thin films and AA monolayers at the air/water interface using XFNTR. Lu[3+] is smaller than La^{3+} and has a higher charge density per unit volume and more surface activity, as demonstrated in other works on rare earth adsorption.[1, 3, 29, 44] XFNTR data (Supporting Information) for GO thin films on LaCl$_3$ and LuCl$_3$ subphases were collected for concentrations ranging from 10 µM to 20 mM and XFNTR data for AA monolayers were collected for concentrations up to 5 mM, as AA is not stable at higher concentrations. For all other measured concentrations, AA exists as a monolayer, as determined by measured pressure-area isotherms (Supporting Information).

The adsorbed La^{3+} and Lu[3+] surface densities are determined (Experimental) and plotted over subphase concentration to create a concentration dependent isotherm (Figure 2), which was fitted to a modified Langmuir adsorption curve (Equation 2). Given that the deprotonated carboxylic acid headgroup of AA has a charge of -1, 3 AA molecules are required per adsorbed ion for charge compensation, which gives a surface charge density of 0.015 ions/Å$^2$ assuming each AA molecule occupies 20 Å$^2$ at the compressed pressure of 10 mN/m (Figure 2, black horizontal line). Reasonably, the AA monolayers achieve charge compensation with adsorbed La^{3+} ions on the 50 µM subphase[1] and retain that adsorbed ion surface density as the subphase concentration increases. GO does not adsorb as many La^{3+} ions, which is consistent with GO having fewer carboxylic acid groups per accessible thin film area as compared to AA, although GO has a more complicated interfacial structure.[24, 25, 28, 29]

Interestingly, $Lu^{3+}$ adsorption onto GO thin films and AA monolayers is quite different (Figure 2). The AA monolayers already achieve charge compensation at the dilute subphase concentrations of 10, 50, and 100 μM $LuCl_3$. The adsorbed $Lu^{3+}$ surface density surpasses this charge compensation value and continues to increase for AA monolayers measured on 500 μM and 5 mM $LuCl_3$ subphases. Evidently, the AA monolayers overcharge at high $LuCl_3$ concentrations, which is likely enabled by enhanced ion-ion correlations for $Lu^{3+}$ due to its ion size compared to $La^{3+}$. Comparing $Lu^{3+}$ adsorption to AA and GO suggests GO also overcharges with $Lu^{3+}$ although GO has a more complicated layered structure at the interface. Overall, XFNTR is a reliable and sensitive probe for determining overcharging because it quantitatively measures the amount of adsorbed metal ion within the interfacial region directly.[3, 39, 40, 45, 48]
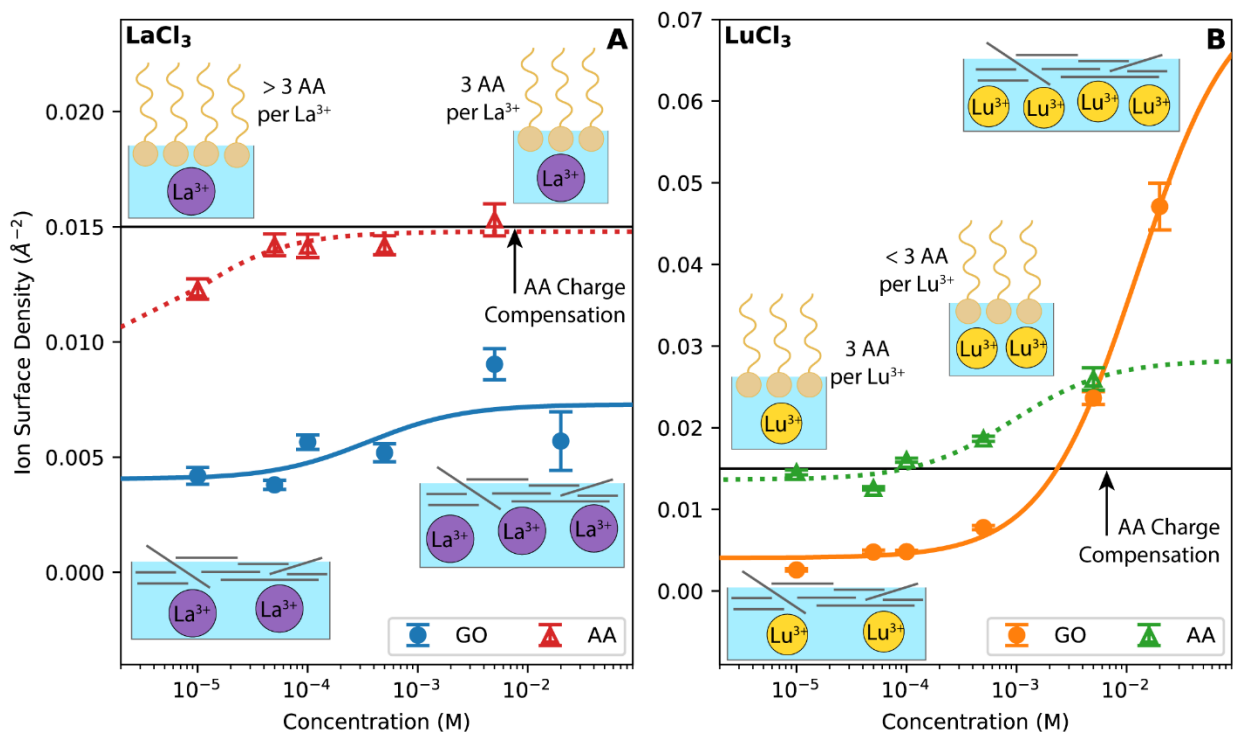


**Figure 2.** Adsorbed ion surface densities for $LaCl_3$ (A) and $LuCl_3$ (B) on graphene oxide thin films (circles) and arachidic acid monolayers (triangles) plotted over subphase concentration. Ion

surface densities were calculated from fitted X-ray fluorescence near total reflection data and error bars are derived from those fits. Obtained ion surface densities were fitted to a modified Langmuir adsorption model (Equation 2). Trivalent ion surface density required for arachidic acid charge compensation is shown (solid black line). Cartoons are not to scale.

*La$^{3+}$ and Lu$^{3+}$ hydration structure during adsorption to graphene oxide and arachidic acid*

To further understand both La$^{3+}$ and Lu$^{3+}$ adsorption to GO and AA, we utilize SFG, an inherently interface specific non-linear spectroscopy technique, to probe the vibrational modes of water.[49] Normalized SFG data collected for GO thin films and AA monolayers on LaCl$_3$ subphases show a dramatic change in SFG intensity as the subphase concentration is increased (Figure 3). The SFG intensity for an AA monolayer on a 50 µM LaCl$_3$ subphase shows low signal, indicating minimal water alignment. This is consistent with the previously presented XFNTR data that show La$^{3+}$ ion adsorption to the monolayer, as adsorbed metal ions disrupt the hydrogen bonding network of the interfacial water and subsequently decrease measured SFG signal.[26, 44, 48] There are two small bands present near approximately 3200 and 3400 cm$^{-1}$, which are generated by aligned, strongly hydrogen bonded water and weakly hydrogen bonded water, respectively.[25, 29, 50] When the subphase concentration is increased to 100 µM LaCl$_3$, a new SFG peak with significant intensity emerges around 3100 cm$^{-1}$. This peak intensity grows for the higher concentration of 500 µM and 5 mM LaCl$_3$. As previously discussed, the XFNTR results show that the amount of adsorbed La$^{3+}$ is nearly constant in this concentration range and is consistent with the ion adsorption values expected for charge compensation, i.e. 1 adsorbed La$^{3+}$ per 3 AA molecules (Figure 2). Together, these data suggest this SFG peak is not induced by ion overcharging, as interpreted previously.[51] Rather, we posit this SFG signal comes from La$^{3+}$ ions that have

undergone partial dehydration during adsorption, consistent with the results of Nayak et al. demonstrated with another light lanthanide, neodymium.[39] The intensity of this SFG peak, which is associated with dehydration, increases as the subphase concentration increases likely because there are more partially dehydrated $La^{3+}$ ions present. We speculate the carboxylic acid groups of AA can facilitate ion dehydration thus encouraging adsorption. These interactions can be assisted by changes in ion-ion correlations with increasing cation concentration. Indeed, multivalent ions are known to disrupt bulk hydration structures.[52] Water structure changes induced by trivalent lanthanides have been observed using Raman spectroscopy[53] and recently with SFG by our group.[39]
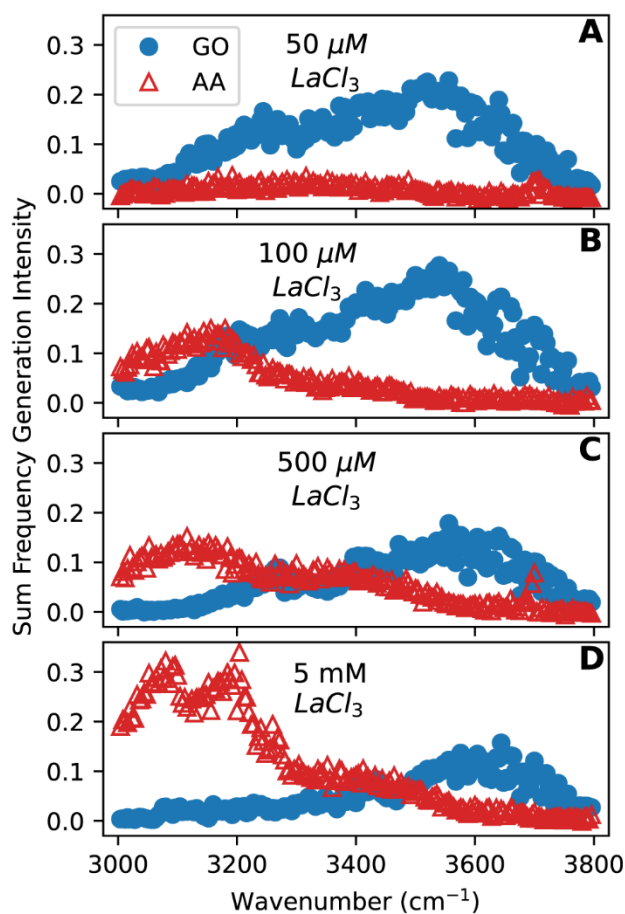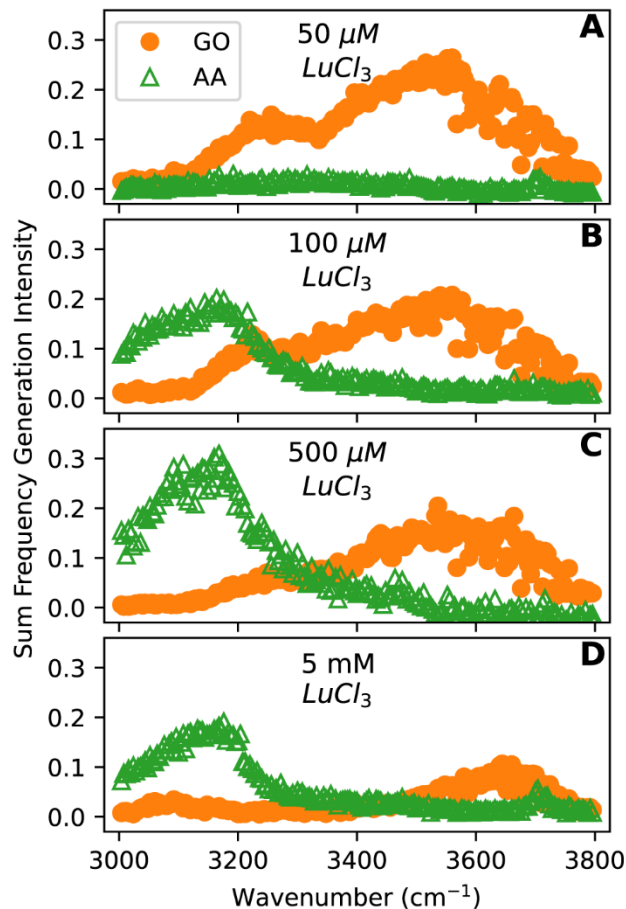


**Figure 3**. Normalized sum frequency generation spectroscopy intensities of the vibrational water region plotted over wavenumber for graphene oxide (GO) thin films (blue circles) and arachidic

13

acid (AA) monolayers (red triangles) on LaCl$_3$ subphases with different concentration (panels). Data are normalized to a reference quartz sample. AA monolayers were compressed to 10 mN/m.

The SFG signal for GO thin films on LaCl$_3$ subphases shows qualitatively different behavior compared to AA. Intense SFG signal is present for films on 50, 100, and 500 μM LaCl$_3$ subphases with two prominent peaks located around 3200 and 3400 cm$^{-1}$, consistent with other works.[23-26, 29] These signals are generated from strongly hydrogen bonded water and weakly hydrogen bonded water, respectively, as discussed earlier. Such large signal is possible because there is little La$^{3+}$ adsorbed to the GO thin film, as determined using XFNTR. With minimal adsorbed metal, water molecules can align thus creating the measurable SFG signal. At 5 mM LaCl$_3$, the measured SFG signal decreases significantly except for a persistent peak around 3600 cm$^{-1}$, attributed to water trapped in between GO flakes within the thin film and thus relatively less affected by metal adsorption.[24, 25, 29] The overall decrease in SFG intensity is consistent with a GO thin film saturated with adsorbed metal.[24, 25] and agrees well with the previous XFNTR results. No significant dehydration signal near 3100 cm$^{-1}$ appears, which implies that not enough partially dehydrated La$^{3+}$ ions adsorb to be detected using SFG.

The measured SFG signal for an AA monolayer on 50 μM LuCl$_3$ subphases (Figure 4) has a low intensity that is similar to the 50 μM LaCl$_3$ subphase (Figure 3). When the subphase concentration is increased to 100 μM LuCl$_3$, a significant peak appears around 3100 cm$^{-1}$ while the remainder of the SFG signal remains low. Like the AA monolayer on LaCl$_3$ subphase SFG results discussed before, we attribute this signal to the partial dehydration of adsorbed Lu$^{3+}$ ions. The absolute SFG intensity for an AA monolayer on 100 μM LuCl$_3$ is slightly larger than the SFG intensity for an AA monolayer on 100 μM LaCl$_3$, which implies more adsorbed Lu$^{3+}$ ions can partially dehydrate

versus the adsorbed $La^{3+}$ ions. This difference in SFG peak intensity is even more pronounced when comparing AA on a 500 μM $LaCl_3$ subphase to AA on a 500 μM $LuCl_3$ subphase. We speculate that more $Lu^{3+}$ ion undergo partial dehydration when compared to $La^{3+}$ because $Lu^{3+}$ has a larger charge density per unit volume due to its smaller size. The $La^{3+}$–O distance for an ion with two layers of hydration[54] is 4.65 Å while the $Lu^{3+}$–O distance[55] is 4.45 Å. $Lu^{3+}$ ions have approximately 2 – 4 fewer water molecules versus $La^{3+}$ in this configuration as well.[56] Consequently, $Lu^{3+}$ has more charge per ion volume compared to $La^{3+}$. This increased charge density more significantly affects local ion-ion correlations and can allow more $Lu^{3+}$ ions to adsorb compared to $La^{3+}$ even though $La^{3+}$ has a more favorable dehydration free energy.[57] Interestingly, the 3100 $cm^{-1}$ peak intensity decreases for the 5 mM $LuCl_3$ subphase. The XFNTR data show that AA is overcharging at this subphase concentration (Figure 2), meaning the 3100 $cm^{-1}$ peak intensity decreases when the monolayer overcharges. This is consistent with the results of Nayak et al. who observed overcharging on AA monolayers when using a light lanthanide and an additional background salt, and a decreased 3100 $cm^{-1}$ SFG signal.[39]

**Figure 4.** Normalized sum frequency generation spectroscopy intensities of the vibrational water region plotted over wavenumber for graphene oxide (GO) thin films (orange circles) and arachidic acid (AA) monolayers (green triangles) on LuCl₃ subphases with different concentration (panels). Data are normalized to a reference quartz sample. AA monolayers were compressed to 10 mN/m.

The measured SFG data for GO thin films on LuCl₃ subphases (Figure 4) show large, bimodal signals for the 50 µM, 100 µM, and 500 µM subphases with a slight decrease in the absolute peak intensity for the 500 µM subphase, consistent with an increase in adsorbed metal ion density, which disrupts local water alignment and decreases SFG signal. The GO thin film on the 5 mM LuCl₃ subphase shows a peak around 3100 cm⁻¹, a signal that has not been observed before for GO thin films at the air/water interface. Consistent with the interpretation of the model AA monolayer SFG

data, we attribute this peak to partially dehydrated, adsorbed metal ions. Previous works have speculated that the functional groups present on GO can facilitate ion adsorption by aiding in dehydration[25] and these SFG data supports these claims. The lack of this signal at the lower LuCl$_3$ subphases does not imply that the adsorbed ions are fully hydrated. Rather, it means the population of dehydrated ions is either too small or not ordered enough to be detected using SFG.

*Graphene oxide and arachidic acid overcharging during Lu$^{3+}$ ion adsorption*

Collectively, the XFNTR and SFG data for both GO thin films and AA monolayers on LaCl$_3$ and LuCl$_3$ subphases can provide detailed information about ion adsorption and water structure at the air/water interface. The previously discussed XFNTR data (Figure 2) for AA monolayers on LaCl$_3$ subphases show about 3.5 – 3.3 AA molecules per adsorbed La$^{3+}$. It is worth noting that XFNTR is not sensitive to the metal hydration structure and can detect metal ions within ~5 nm of the liquid surface.[45] Using a La$^{3+}$–O bond distance, determined experimentally with X-ray scattering,[54] of 4.65 Å, one would expect a geometric maximum of 3.4 AA molecules per La$^{3+}$ if the metal ion retains both layers of its hydration shell. This geometric limit is not a favorable configuration for adsorbed ions, meaning it is likely some of adsorbed La$^{3+}$ detected using XFNTR have undergone partial dehydration while adsorbing to the AA monolayer. This interpretation is consistent with the SFG results showing signal from an ordered population of partially dehydrated metal ions.

Similar calculations for AA monolayers on LuCl$_3$ subphases support monolayer overcharging where ions continue to adsorb to the monolayer even after the system achieves charge compensation. From the XFNTR data presented above (Figure 2), the calculated AA molecule per adsorbed Lu$^{3+}$ ion is ~3.1 for a 100 μM LuCl$_3$ subphase and decreases to about 1.9 for a 5 mM

LuCl$_3$ subphase, indicating significant overcharging. The geometric upper limit of these adsorbed Lu$^{3+}$ ions is about 3.1 AA molecules per ion if the metal retains both layers of its hydration shell. This physical limit decreases to about 0.86 AA molecules per adsorbed Lu$^{3+}$ if the Lu$^{3+}$ shed the outermost hydration shell thus decreasing the Lu$^{3+}$–O distance[55] to 2.34 Å. Because such geometric limits are not favorable configurations, these results imply a portion of Lu$^{3+}$ ions partially dehydrate while adsorbing to an AA monolayer on a 100 µM LuCl$_3$ subphase. Given the amount of adsorbed Lu$^{3+}$ ion in the 5 mM subphase case, it is not possible for all adsorbed ions to retain two full hydration shells. Instead, some Lu$^{3+}$ ions must shed part of their water structure. These calculations agree well with the SFG results that show a red-shifted peak in the vibrational water region for AA monolayers on LuCl$_3$ subphases, indicating metal ion partial dehydration. Dehydration is necessary for these monolayers to accommodate the excess metal ions present during overcharging.

Interestingly, the amount of adsorbed Lu$^{3+}$ to GO is similar to that of AA for a 5 mM LuCl$_3$ subphase even though GO has a much smaller surface charge because it has less carboxylic acid groups per unit area compared to AA. Another work by our group estimated the GO is about 8% carboxylic acid, as determined using *ex situ* X-ray photoelectron spectroscopy and *in situ* SFG.[26] However, unlike AA, GO under these experimental conditions is not a monolayer and instead has a complicated, multilayer structure at the air/water interface.[24, 29] We use XR to determine the GO film structure with sub-nanometer resolution.

XR data on GO thin films on 50 µM LaCl$_3$ and LuCl$_3$ subphases are nearly identical with two features near $Q_Z$ = 0.11 and 0.31 Å$^{-1}$ (Figure 5). Fitting to a three slab model gives an electron density profile consistent with previous results.[24, 29] We interpret this profile as one layer of GO flakes is partially submerged in the subphase, one layer sits at the air/water interface, and the last

layer pushes up into the air. GO film on plain water does not show a partially submerged layer, which implies the GO layer closest to the liquid interacts primarily with adsorbed metal ions. The electron density profiles for the films on 50 μM $LaCl_3$ and $LuCl_3$ are similar because at this subphase concentration, a similar number of ions adsorb. Taken together with the XFNTR data, these data demonstrate that GO thin films show no specificity between light and heavy lanthanide ions at dilute concentrations. This implies that at low subphase concentrations, ion-ion correlations are not significant enough to overcome energetically unfavorable steric hindrance between adsorbed cations. Presumably, the functional groups of GO still enable ion dehydration but electrostatic repulson between the cations hinders adsorption.

XR data for a GO film on a 20 mM $LuCl_3$ are significantly different with more prominent signal at $Q_Z \sim 0.1$ and $0.3$ $Å^{-1}$ and additional features at $Q_Z = 0.4$ and $0.57$ $Å^{-1}$ (Figure 5). Consequently, the electron density profile shows higher density after fitting with a three slab model. Integrating these electron density profiles gives an electron density per unit area.[29] The integrated electron density profile for a GO thin film on a 20 mM $LuCl_3$ subphase shows an excess $\sim 1.4$ $e^-/Å^2$ after accounting for electrons from the GO thin film on plain water (i.e. electron density from the GO itself and electron density from water typically near the GO film) and electrons from the adsorbed $Lu^{3+}$ ions. This extra electron density likely stems from additional water surrounding the adsorbed ions at the interface, which is present in much smaller amounts for films made on lower concentration subphases, consistent with the differences in adsorbed ion densities.
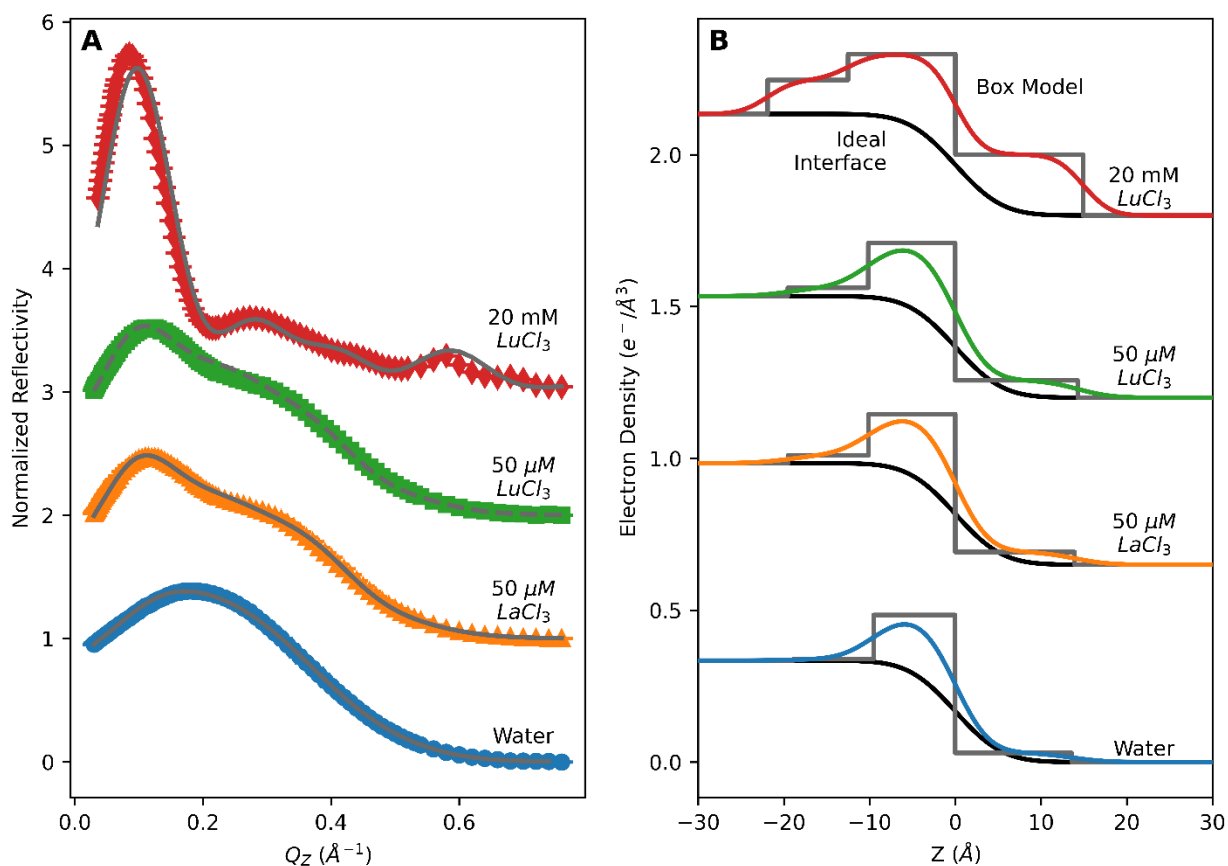
**Figure 5.** Normalized liquid surface X-ray reflectivity and fits (gray lines) plotted over momentum transfer $Q_Z$ (A) of graphene oxide thin films on different subphases (colors) and calculated electron density profiles from fitted reflectivity data (B). The corresponding box model with no roughness (gray) and an ideal interface (black) are included.

Comparing the AA and GO results for $LuCl_3$ subphases allows us to demonstrate GO overcharging. An ideal monolayer of AA requires 0.015 adsorbed $Lu^{3+}/Å^2$ to achieve charge compensation (Figure 4). Considering that the carboxylic acid density of GO is around 8% of AA, 0.0012 $Lu^{3+}/Å^2$ would compensate the surface charge of GO. XFNTR data for a GO thin film on 20 mM $LuCl_3$ subphase has an adsorbed ion density of 0.047 ± 0.003 $Lu^{3+}/Å^2$, which is significantly higher than the amount needed for charge compensation of an AA monolayer. XR data for a GO film on this subphase show significantly more electron density within the two layers

closest to the liquid surface, meaning adsorbed $Lu^{3+}$ ions are not distributed evenly across the GO layers. Taken together, these data suggest GO overcharges on significantly concentrated $LuCl_3$ subphases. We speculate GO thin films can accommodate more adsorbed $Lu^{3+}$ ions than necessary for charge compensation because of their layered structure. It is possible the GO flakes can rearrange to minimize electrostatic repulsion between adsorbed cations, which is also reduced by the subphase concentration. This can be contrasted to the overcharging of $Y^{3+}$ on pristine graphene surface, where the $Y^{3+}$ ions could not dehydrate and form a very diffuse layer.[58] It is also possible that the GO itself can chemically rearrange to accommodate adsorbed $Lu^{3+}$ ions. David and Kumar show via Born-Oppenheimer molecular dynamics that GO flakes can react with pure water and form different functional groups, depending on the GO degree of oxidation.[59] It follows that GO flakes can also move protons in response to adsorbed cations. AA monolayers do not have such flexibility and therefore cannot accommodate more adsorbed ions even with improved ion-ion correlations.

**Conclusions**

Isolating targeted lanthanide ions from mixtures is imperative for many high technology applications but challenging, due to the chemical similarities across the lanthanide series. In this work, we investigate the effects of lanthanide size on ion adsorption to GO thin films and AA monolayers at the air/water interface using $La^{3+}$ and $Lu^{3+}$. Interface-specific XFNTR provides quantitative adsorbed ion densities and shows $Lu^{3+}$ overcharges when adsorbing to AA and GO on higher concentration subphases. $La^{3+}$ adsorption is consistent with the expected charge compensation, 1 trivalent metal ion per 3 deprotonated carboxylic acid headgroups. Determining the surface charge of GO is difficult, as GO forms a multilayer thin film at the air/water interface. XR data show 3 primary layers within the GO thin film with most of the electron density existing

in the layers closest to the liquid surface. When combined with the adsorbed ion densities obtained by XFNTR, this data supports GO overcharging.

Additional SFG data reveal the hydration structure of the adsorbed ions to both AA and GO. The emergence of a red-shifted signal in the vibrational water region for AA is attributed to partial ion dehydration. Both light $La^{3+}$ and heavy $Lu^{3+}$ show this peak, meaning it is not related to monolayer overcharging. Rather, the peak intensity decreases slightly as more ions adsorb, possibly because these extra adsorbed ions disrupt local water alignment and SFG detection. This dehydration peak is also present for a GO thin film on a high concentration $Lu^{3+}$ subphase, which supports the argument that GO functional groups enable significant ion adsorption by facilitating ion dehydration. Taken together, these results underscore the importance of considering model monolayers in comparison to more complicated, but technologically relevant, GO thin films and highlight the necessity of multiple surface probes to detail the interface.

## ASSOCIATED CONTENT

**Supporting Information**. Pressure-area isotherms for arachidic acid monolayers, parameters for fitted X-ray reflectivity data, X-ray fluorescence near total reflection data for graphene oxide and arachidic acid.

## AUTHOR INFORMATION

**Corresponding Author**

*Corresponding Author: AU, Email: ahmet@anl.gov, Phone: +1-630-252-9133

**Author Contributions**

The manuscript was written through contributions of all authors. All authors have given approval to the final version of the manuscript.

REFERENCES

1.    Miller, M.;  Liang, Y.;  Li, H.;  Chu, M.;  Yoo, S.;  Bu, W.;  Olvera de la Cruz, M.; Dutta, P., Electrostatic Origin of Element Selectivity during Rare Earth Adsorption. *Phys. Rev. Lett.* **2019,** *122* (5), 058001.

2.    Xie, F.;  Zhang, T. A.;  Dreisinger, D.; Doyle, F., A critical review on solvent extraction of rare earths from aqueous solutions. *Miner. Eng.* **2014,** *56*, 10-28.

3.    Sun, P.;  Binter, E. A.;  Liang, Z.;  Brown, M. A.;  Gelis, A. V.;  Benjamin, I.;  Bera, M. K.;  Lin, B.;  Bu, W.; Schlossman, M. L., Antagonistic Role of Aqueous Complexation in the Solvent Extraction and Separation of Rare Earth Ions. *ACS Cent. Sci* **2021,** *7* (11), 1908-1918.

4.      Martinez-Gomez, N. C.;   Vu, H. N.;  Skovran, E., Lanthanide Chemistry: From Coordination in Chemical Complexes Shaping Our Technology to Coordination in Enzymes Shaping Bacterial Metabolism. *Inorg. Chem.* **2016,** *55* (20), 10083-10089.

5.      Liu, G.;   Jin, W.;  Xu, N., Graphene-based membranes. *Chem. Soc. Rev.* **2015,** *44* (15), 5016-30.

6.      Lerf, A.;   He, H.;   Forster, M.;  Klinowski, J., Structure of Graphite Oxide Revisited. *J. Phys. Chem. B* **1998,** *102* (23), 4477-4482.

7.      Hidalgo, R. S.;   Lopez-Diaz, D.;  Velazquez, M. M., Graphene oxide thin films: influence of chemical structure and deposition methodology. *Langmuir* **2015,** *31* (9), 2697-705.

8.      Chen, J.;   Chi, F.;   Huang, L.;   Zhang, M.;   Yao, B.;   Li, Y.;   Li, C.;  Shi, G., Synthesis of graphene oxide sheets with controlled sizes from sieved graphite flakes. *Carbon* **2016,** *110*, 34-40.

9.      Krishnamoorthy, K.;   Veerapandian, M.;   Yun, K.;  Kim, S. J., The chemical and structural analysis of graphene oxide with different degrees of oxidation. *Carbon* **2013,** *53*, 38-49.

10.    Hu, B.;   Hu, Q.;   Li, X.;   Pan, H.;   Tang, X.;   Chen, C.;  Huang, C., Rapid and highly efficient removal of Eu(III) from aqueous solutions using graphene oxide. *J. Mol. Liq.* **2017,** *229*, 6-14.

11.    Xie, Y.;   Helvenston, E. M.;   Shuller-Nickles, L. C.;  Powell, B. A., Surface Complexation Modeling of Eu(III) and U(VI) Interactions with Graphene Oxide. *Environ. Sci. Technol.* **2016,** *50* (4), 1821-7.

12.    Chang, K.;   Sun, Y.;   Ye, F.;   Li, X.;   Sheng, G.;   Zhao, D.;   Linghu, W.;   Li, H.;  Liu, J., Macroscopic and molecular study of the sorption and co-sorption of graphene oxide and Eu(III) onto layered double hydroxides. *Chem. Eng. J.* **2017,** *325*, 665-671.

13.    Peng, W.;  Li, H.;  Liu, Y.; Song, S., A review on heavy metal ions adsorption from water by graphene oxide and its composites. *J. Mol. Liq.* **2017,** *230*, 496-504.

14.    Boulanger, N.;  Kuzenkova, A. S.;  Iakunkov, A.;  Romanchuk, A. Y.;  Trigub, A. L.; Egorov, A. V.;  Bauters, S.;  Amidani, L.;  Retegan, M.;  Kvashnina, K. O.;  Kalmykov, S. N.; Talyzin, A. V., Enhanced Sorption of Radionuclides by Defect-Rich Graphene Oxide. *ACS Appl. Mater. Interfaces* **2020,** *12* (40), 45122-45135.

15.    Kuzenkova, A. S.;  Romanchuk, A. Y.;  Trigub, A. L.;  Maslakov, K. I.;  Egorov, A. V.; Amidani, L.;  Kittrell, C.;  Kvashnina, K. O.;  Tour, J. M.;  Talyzin, A. V.; Kalmykov, S. N., New insights into the mechanism of graphene oxide and radionuclide interaction. *Carbon* **2020,** *158*, 291-302.

16.    Romanchuk, A. Y.;  Slesarev, A. S.;  Kalmykov, S. N.;  Kosynkin, D. V.; Tour, J. M., Graphene oxide for effective radionuclide removal. *Phys. Chem. Chem. Phys.* **2013,** *15* (7), 2321-7.

17.    Xie, Y.; Powell, B. A., Linear Free Energy Relationship for Actinide Sorption to Graphene Oxide. *ACS Appl. Mater. Interfaces* **2018,** *10* (38), 32086-32092.

18.    Mohamud, H.;  Ivanov, P.;  Russell, B. C.;  Regan, P. H.; Ward, N. I., Selective sorption of uranium from aqueous solution by graphene oxide-modified materials. *J. Radioanal. Nucl. Chem.* **2018,** *316* (2), 839-848.

19.    Khaliha, S.;  Marforio, T. D.;  Kovtun, A.;  Mantovani, S.;  Bianchi, A.;  Luisa Navacchia, M.;  Zambianchi, M.;  Bocchi, L.;  Boulanger, N.;  Iakunkov, A.;  Calvaresi, M.;  Talyzin, A. V.;

Palermo, V.; Melucci, M., Defective graphene nanosheets for drinking water purification: Adsorption mechanism, performance, and recovery. *FlatChem* **2021,** *29*, 100283.

20. Nguyen, M. T.; Zhang, J.; Prabhakaran, V.; Tan, S.; Baxter, E. T.; Shutthanandan, V.; Johnson, G. E.; Rousseau, R.; Glezakou, V. A., Graphene Oxide as a Pb(II) Separation Medium: Has Part of the Story Been Overlooked? *JACS Au* **2021,** *1* (6), 766-776.

21. Romaniak, G.; Dybowski, K.; Jeziorna, A.; Kula, P.; Kaźmierczak, T., Synthesis and characterization of semi-permeable graphene/graphene oxide membranes for water desalination. *J. Mater. Sci.* **2020,** *55* (23), 9775-9786.

22. Kaewmee, P.; Manyam, J.; Opaprakasit, P.; Truc Le, G. T.; Chanlek, N.; Sreearunothai, P., Effective removal of cesium by pristine graphene oxide: performance, characterizations and mechanisms. *RSC Advances* **2017,** *7* (61), 38747-38756.

23. Hong, Y.; He, J.; Zhang, C.; Wang, X., Probing the Structure of Water at the Interface with Graphene Oxide Using Sum Frequency Generation Vibrational Spectroscopy. *J. Phys. Chem. C* **2022,** *126* (3), 1471-1480.

24. Kumal, R.; Carr, A. J.; Uysal, A., A Simple Method for High-Quality Ultra-Thin Graphene Oxide Films Facilitates Nanoscale Investigations of Ion and Water Adsorption. *ChemRxiv* **2022**, DOI: 10.26434/chemrxiv-2022-1csxr.

25. Carr, A. J.; Kumal, R. R.; Bu, W.; Uysal, A., Effects of ion adsorption on graphene oxide films and interfacial water structure: A molecular-scale description. *Carbon* **2022,** *195*, 131-140.

26.    Lee, S. E.;  Carr, A. J.;  Kumal, R. R.;  Uysal, A., Monovalent Ion-Graphene Oxide Interactions are Controlled by Carboxylic Acid Groups: Sum Frequency Generation Spectroscopy Studies. *ChemRxiv* **2023**, DOI: 10.26434/chemrxiv-2023-dj4m0-v2.

27.    López-Díaz, D.;  Merchán, M. D.;  Velázquez, M. M.; Maestro, A., Understanding the Role of Oxidative Debris on the Structure of Graphene Oxide Films at the Air–Water Interface: A Neutron Reflectivity Study. *ACS Appl. Mater. Interfaces* **2020,** *12* (22), 25453-25463.

28.    Bonatout, N.;  Muller, F.;  Fontaine, P.;  Gascon, I.;  Konovalov, O.; Goldmann, M., How exfoliated graphene oxide nanosheets organize at the water interface: evidence for a spontaneous bilayer self-assembly. *Nanoscale* **2017,** *9* (34), 12543-12548.

29.    Carr, A. J.;  Lee, S. E.;  Kumal, R. R.;  Bu, W.; Uysal, A., Convenient Confinement: Interplay of Solution Conditions and Graphene Oxide Film Structure on Rare Earth Separations. *ACS Appl. Mater. Interfaces* **2022,** *14* (51), 57133-57143.

30.    Johnson, K. R.;  Driscoll, D. M.;  Damron, J. T.;  Ivanov, A. S.; Jansone-Popova, S., Size Selective Ligand Tug of War Strategy to Separate Rare Earth Elements. *JACS Au* **2023**, DOI: 10.1021/jacsau.2c00671.

31.    Ellis, R. J.;  Brigham, D. M.;  Delmau, L.;  Ivanov, A. S.;  Williams, N. J.;  Vo, M. N.; Reinhart, B.;  Moyer, B. A.; Bryantsev, V. S., "Straining" to Separate the Rare Earths: How the Lanthanide Contraction Impacts Chelation by Diglycolamide Ligands. *Inorg. Chem.* **2017,** *56* (3), 1152-1160.

32.    Li, Z.; Binnemans, K., Hydration counteracts the separation of lanthanides by solvent extraction. *AlChE J.* **2020,** *66* (9), e16545.

33. Ferru, G.; Reinhart, B.; Bera, M. K.; Olvera de la Cruz, M.; Qiao, B.; Ellis, R. J., The Lanthanide Contraction beyond Coordination Chemistry. *Chem. Eur. J.* **2016,** *22* (20), 6899-904.

34. Duvail, M.; Spezia, R.; Vitorge, P., A dynamic model to explain hydration behaviour along the lanthanide series. *ChemPhysChem* **2008,** *9* (5), 693-6.

35. Qiao, B.; Skanthakumar, S.; Soderholm, L., Comparative CHARMM and AMOEBA Simulations of Lanthanide Hydration Energetics and Experimental Aqueous-Solution Structures. *J. Chem. Theory Comput.* **2018,** *14* (3), 1781-1790.

36. Allen, P. G.; Bucher, J. J.; Shuh, D. K.; Edelstein, N. M.; Craig, I., Coordination chemistry of trivalent lanthanide and actinide ions in dilute and concentrated chloride solutions. *Inorg. Chem.* **2000,** *39* (3), 595-601.

37. Rizkalla, E. N.; Choppin, G. R., Hydration of lanthanides and actinides in solution. *J. Alloys Compd.* **1992,** *180* (1-2), 325-336.

38. Miller, M.; Chu, M.; Lin, B.; Bu, W.; Dutta, P., Atomic Number Dependent "Structural Transitions" in Ordered Lanthanide Monolayers: Role of the Hydration Shell. *Langmuir* **2017,** *33* (6), 1412-1418.

39. Nayak, S.; Kumal, R. R.; Lee, S. E.; Uysal, A., Elucidating Trivalent Ion Adsorption at Floating Carboxylic Acid Monolayers: Charge Reversal or Water Reorganization? *ChemRxiv* **2023**, DOI: 10.26434/chemrxiv-2023-n278x.

40. Nayak, S.; Kumal, R. R.; Liu, Z.; Qiao, B.; Clark, A. E.; Uysal, A., Origins of Clustering of Metalate-Extractant Complexes in Liquid-Liquid Extraction. *ACS Appl. Mater. Interfaces* **2021,** *13* (20), 24194-24206.

41. Rock, W.; Qiao, B.; Zhou, T.; Clark, A. E.; Uysal, A., Heavy Anionic Complex Creates a Unique Water Structure at a Soft Charged Interface. *J. Phys. Chem. C* **2018,** *122* (51), 29228-29236.

42. Kumal, R. R.; Wimalasiri, P. N.; Servis, M. J.; Uysal, A., Thiocyanate Ions Form Antiparallel Populations at the Concentrated Electrolyte/Charged Surfactant Interface. *J. Phys. Chem. Lett.* **2022,** *13* (22), 5081-5087.

43. Lovering, K.; Nayak, S.; Bu, W.; Uysal, A., The Role of Specific Ion Effects in Ion Transport: The Case of Nitrate and Thiocyanate. *J. Phys. Chem. C* **2019,** *124*, 573-581.

44. Nayak, S.; Kumal, R. R.; Uysal, A., Spontaneous and Ion-Specific Formation of Inverted Bilayers at Air/Aqueous Interface. *Langmuir* **2022,** *38* (18), 5617-5625.

45. Bera, M. K.; Bu, W.; Uysal, A., Liquid surface x-ray scattering. In *Physical Chemistry of Gas-Liquid Interfaces*, Faust, J.; House, J., Eds. Elsevier: 2018; pp 167-194.

46. Danauskas, S. M.; Li, D. X.; Meron, M.; Lin, B. H.; Lee, K. Y. C., Stochastic fitting of specular X-ray reflectivity data using StochFit. *Journal of Applied Crystallography* **2008,** *41* (6), 1187-1193.

47. Schmidt, M.; Lee, S. S.; Wilson, R. E.; Soderholm, L.; Fenter, P., Sorption of tetravalent thorium on muscovite. *Geochim. Cosmochim. Acta* **2012,** *88*, 66-76.

48. Kumal, R. R.; Nayak, S.; Bu, W.; Uysal, A., Chemical Potential Driven Reorganization of Anions between Stern and Diffuse Layers at the Air/Water Interface. *J. Phys. Chem. C* **2022,** *126* (2), 1140-1151.

49.    Johnson, C. M.; Baldelli, S., Vibrational Sum Frequency Spectroscopy Studies of the Influence of Solutes and Phospholipids at Vapor/Water Interfaces Relevant to Biological and Environmental Systems. *Chem. Rev.* **2014,** *114* (17), 8416-8446.

50.    Geiger, F. M., Second harmonic generation, sum frequency generation, and chi(3): dissecting environmental interfaces with a nonlinear optical Swiss Army knife. *Annu. Rev. Phys. Chem.* **2009,** *60*, 61-83.

51.    Sthoer, A.;  Adams, E. M.;  Sengupta, S.;  Corkery, R. W.;  Allen, H. C.; Tyrode, E. C., La3+ and Y3+ interactions with the carboxylic acid moiety at the liquid/vapor interface: Identification of binding complexes, charge reversal, and detection limits. *J. Colloid Interface Sci.* **2022,** *608*, 2169-2180.

52.    Roy, S.;  Patra, A.;  Saha, S.;  Palit, D. K.; Mondal, J. A., Restructuring of Hydration Shell Water due to Solvent-Shared Ion Pairing (SSIP): A Case Study of Aqueous MgCl(2) and LaCl(3) Solutions. *J. Phys. Chem. B* **2020,** *124* (37), 8141-8148.

53.    Patra, A.;  Roy, S.;  Saha, S.;  Palit, D. K.; Mondal, J. A., Observation of Extremely Weakly Interacting OH (∼3600 cm–1) in the Vicinity of High Charge Density Metal Ions (Mz+; z = 1, 2, 3): A Structural Heterogeneity in the Extended Hydration Shell. *J. Phys. Chem. C* **2020,** *124* (5), 3028-3036.

54.    Habenschuss, A.; Spedding, F. H., The coordination (hydration) of rare earth ions in aqueous chloride solutions from X-ray diffraction. II. LaCl3, PrCl3, and NdCl3. *J. Chem. Phys.* **1979,** *70* (8), 3758-3763.

55.    Habenschuss, A.; Spedding, F. H., The coordination (hydration) of rare earth ions in aqueous chloride solutions from X-ray diffraction. I. TbCl3, DyCl3, ErCl3, TmCl3, and LuCl3. *J. Chem. Phys.* **1979,** *70* (6), 2797-2806.

56.    Smirnov, P. R.; Trostin, V. N., Structural parameters of close surroundings of Sr2+ and Ba2+ ions in aqueous solutions of their salts. *Russ. J. Gen. Chem.* **2011,** *81* (2), 282-289.

57.    Marcus, Y., A simple empirical model describing the thermodynamics of hydration of ions of widely varying charges, sizes, and shapes. *Biophys. Chem.* **1994,** *51* (2-3), 111-127.

58.    Carr, A. J.;  Lee, S. S.; Uysal, A., Trivalent ion overcharging on electrified graphene. *J. Phys.: Condens. Matter* **2022,** *34* (14), 144001.

59.    David, R.; Kumar, R., Reactive events at the graphene oxide-water interface. *Chem. Commun.* **2021,** *57* (88), 11697-11700.

**TOC GRAPHIC**